

**Numerical Assessment of SOFC Anode Polarization Based on Three-Dimensional Model
Microstructure Reconstructed from FIB-SEM Images**

Naoki Shikazono, Daisuke Kanno, Katsuhisa Matsuzaki, Hisanori Teshima, Shinji Sumino and
Nobuhide Kasagi

Keywords: Lattice Boltzmann method, SOFC anode, Focused ion beam scanning electron microscopy

Department of Mechanical Engineering, The University of Tokyo, Hongo 7-3-1, Bunkyo-ku, Tokyo
113-8656, Japan

Abstract

A three-dimensional numerical simulation of the anode overpotential is conducted in a microstructure which is reconstructed by a dual-beam focused ion beam-scanning electron microscope. Gaseous, ionic and electronic transport equations are solved by a lattice Boltzmann method with electrochemical reaction at the three-phase boundary. The predicted anode overpotential shows good agreement with the experimental data at the fuel supply of 1.2% H₂O - 98.8% H₂, while it is larger than the data at 10% H₂O - 90% H₂. The dependence of exchange current density on steam partial pressure, gas diffusion modeling as well as computational domain size must be further investigated in the future. Local three-dimensional distributions of electrochemical potential and current density inside the anode microstructure are obtained. Their non-uniformities are attributed to the scattered three-phase boundaries and complex transport paths through the solid phases.

Introduction

Solid oxide fuel cell (SOFC) is anticipated to play a major role in the future energy utilization because of its superior efficiency and fuel flexibility.¹ However, its cost effectiveness and durability must be further improved before market introduction. It is widely known that the electrode microstructure has significant effects upon the cell performance and durability of SOFCs. Thus, the basic understanding of microscopic features of the electrode is indispensable. Quantitative investigations which relate the electrode microstructural parameters obtained from two-dimensional images and the polarization resistances have been reported. Wilson and Barnett² related anode polarization resistances to the three phase boundary (TPB) densities of Ni-YSZ active layers by means of stereology. Shikazono et al.³ also used stereology as well as concept of contiguity (CC) theory to investigate the relationship between the polarization characteristics and the microstructural parameters such as TPB length and effective conductivities. However, a random mixture is assumed in stereology and CC theory, which has to be validated for further investigation. Furthermore, dead ends of the phases and electrochemically inactive TPBs should be rationally removed for quantitatively discussing the effects of microstructure on polarization characteristics. In order to overcome these issues, it is necessary to establish a method which can directly predict the polarization resistance in the real three-dimensional microstructure.

Recently, direct measurements of three-dimensional SOFC electrode microstructure have been carried out using focused ion beam scanning electron microscopy (FIB-SEM)⁴⁻¹⁰ and X-ray computed tomography (XCT).¹¹ As a result, useful quantitative data such as TPB length and tortuosity factor are obtained from the reconstructed three-dimensional microstructures. However, a difficulty still remains in removing errors which arise from discretization process and insufficient sample volume size.^{9, 10, 12}

In addition to the above experimental studies, numerical simulations have possibilities to provide useful information which cannot be obtained from experiments. Recently, much attention has been paid to the lattice Boltzmann method (LBM), which is suitable for simulating complicated multi-phase porous electrodes. Joshi et al.¹³ performed a multi-component LBM simulation in a two dimensional porous media. Asinari et al.¹⁴ also used a LBM for solving H₂ and H₂O diffusion inside

the micro pores. Suzue et al.¹⁵ conducted a three-dimensional LBM simulation in a stochastically reconstructed anode structure. It was the first LBM work to solve the species transport coupled with the electrochemical reaction at TPB in a three-dimensional SOFC anode. However, their microstructure was not real, but reconstructed by a stochastic reconstruction scheme proposed by Yeong and Torquato¹⁶. In contrast, Chiu et al.¹⁷ performed LBM simulation using an anode structure reconstructed from XCT images, and showed two-dimensional mass transfer results, but electrochemically active TPB sites were not incorporated in their simulation. In order to assess the applicability of such numerical simulation, it is mandatory to compare the predicted polarization characteristics directly with the experimental data.

From the above, it is clear that numerical simulation should be made with an identical electrode microstructure which is used in the polarization experiment. In the present study, three-dimensional microstructure of an anode measured by a dual-beam focused ion beam-scanning electron microscopy (FIB-SEM)¹⁰ is used for the numerical simulation. The anode overpotential is then calculated by the LBM solving the species-transport coupled with the electrochemical reaction at TPB. In order to calculate the TPB length accurately from discretized voxel data, a simple method based on centroids of neighboring TPB midpoints is proposed. Predicted overpotential is compared with the experimental data¹⁸ for validation. Furthermore, the three-dimensional distributions of electrochemical potential and current density are presented.

Reconstructed Microstructure Using FIB-SEM

The sample used in this study is the Ni-YSZ cermet anode (Ni:YSZ = 50:50 vol%) which is reconstructed by FIB-SEM in our previous work.¹⁰ The anode was sintered at 1400 °C for 5 hours and reduced at 1000 °C. The sample was infiltrated with epoxy resin (Marumoto Struers KK) under vacuum conditions so that the pores of the porous electrode could be easily distinguished during SEM observation. Cured sample was polished using an Ar-ion beam cross-section polisher (JEOL Ltd., SM-09010) and made available for the FIB-SEM (Carl Zeiss, NVision 40) observation. Cross-sectional images (26 nm/pixel) are obtained at a 62 nm interval. The volume size is 18.60 × 8.43 × 6.20 μm³. Pore, Ni and YSZ phases are distinguished by their brightness values. Then, three-

dimensional microstructure is re-meshed to 62 nm cubic voxels for the numerical analysis. Figure 1 shows an example of the phase distinguished cross-sectional image. The reconstructed three-dimensional microstructure is shown in Fig. 2.

Numerical Method

Computational Domain

For securing a sufficiently large electrode thickness, five mirrored FIB-SEM structures are repeated in the z direction as shown in Fig. 3. The electrolyte-anode interface is set at $z = 0 \mu\text{m}$, while the anode-current collector (CC) interface at $z = 31 \mu\text{m}$. The thicknesses of electrolyte and CC layers are 1.302 and 0.62 μm , respectively.

Three-phase boundary length

In the present study, TPB length is calculated as follows. If the neighboring four cubic voxels comprise all three phases with different phases in two diagonal voxels, the edge surrounded by the four voxels is defined as a TPB segment. One of the possible voxel arrangements and the corresponding TPB segments are shown in Fig. 4a. If the lengths of TPB segments are simply summed, it is apparent that the total TPB length would be overestimated because of the inevitable step-like pattern of voxel edges. Suzue et al.¹⁵ assumed that TPB length was 20 % smaller than the value directly calculated from the cubic voxel perimeter of reconstructed structure. Golbert et. al.¹² counted the number of all the voxels neighboring a TPB edge (four per edge) and divided the overall number by four to obtain the total number of effective TPB edges. This approach reduces calculated TPB length because some voxels contain more than one TPB edge, but are only counted once. However, non-intuitive approach is desired for calculating TPB length, since TPB length is one of the most important parameters for predicting electrode polarization characteristics.

In the present study, three methods to calculate TPB length from voxel edge segments are compared. The first method is a simple summation of voxel edge segments as shown in Fig. 4b. The second method defines the connection length of the midpoints of the TPB edge segments (Fig. 4c), whereas the third gives the total distance between the centroids of the triangles defined by the

neighboring midpoints of the edge segments (Fig. 4d). These three methods are compared by applying them to a structure with well defined TPB, i.e. two overlapped spheres.

As shown in Fig. 5, TPB length can be analytically obtained from this configuration. The radius of the sphere r and the distance between two centers l are varied. Overlap ratio c is defined as:

$$c = 1 - \frac{l}{2r}. \quad [1]$$

Figure 6 shows the difference between the calculated TPB lengths and the analytical value for three different radius to voxel size ratios, $r/\Delta x$. The symbols in the figure represent the mean values from 500 randomly chosen sphere positions for given radius and overlap ratio, and the bars are the standard deviations. It is evident that the simple summation of edge segments overestimates TPB length more than 50%. On the other hand, the centroid method can predict TPB length within 5% error in most cases. If $r/\Delta x$ is small, i.e., if grid resolution is not high enough, variation of TPB length becomes considerably large.

The TPB lengths calculated from the FIB-SEM images are listed in Table I. The TPB length calculated by simple edge summation gives $3.964 \mu\text{m}/\mu\text{m}^3$, while the centroid method gives $2.556 \mu\text{m}/\mu\text{m}^3$. The latter result agrees very well with the volume expansion method¹⁰, which gives $2.487 \mu\text{m}/\mu\text{m}^3$. The centroid method is employed for the rest of this study.

Governing Equations

Gaseous, electronic and ionic diffusion equations are solved inside each of the obtained three-dimensional Ni, YSZ and pore phases. In the gaseous phase, hydrogen and steam diffusion is solved based on a dusty gas model (DGM).¹⁹ If a constant total pressure is assumed, DGM is generally written as follows:

$$\frac{N_i}{D_{i,k}} + \sum_{j \neq i} \frac{y_j N_i - y_i N_j}{D_{i,j}} = -\frac{1}{RT} \nabla p_i, \quad [2]$$

where y_i is the molar fraction, N_i is the molar flux, and p_i is the partial pressure. Subscripts i and j represent gas species such as hydrogen and steam. In the present study, binary (H_2 and H_2O) equimolar diffusion in a constant total pressure p_t environment is assumed, i.e.,

$$p_t = p_{\text{H}_2\text{O}} + p_{\text{H}_2} . \quad [3]$$

Therefore, only the diffusion equation of hydrogen is solved:

$$\nabla \left(\left[\frac{1 - \alpha y_{\text{H}_2}}{D_{\text{H}_2, \text{H}_2\text{O}}} + \frac{1}{D_{\text{H}_2, \text{k}}} \right]^{-1} \nabla C_{\text{H}_2} \right) = \frac{i_{\text{react}}}{2F} , \quad [4]$$

where C_{H_2} is the molar concentration of hydrogen gas with

$$\alpha = 1 - \left(\frac{M_{\text{H}_2}}{M_{\text{H}_2\text{O}}} \right)^{1/2} . \quad [5]$$

In Eq. 4, $D_{\text{H}_2, \text{H}_2\text{O}}$ and $D_{\text{H}_2, \text{k}}$ represent the binary and Knudsen diffusion coefficients, respectively:

$$D_{\text{H}_2, \text{H}_2\text{O}} = 0.018833 \sqrt{\frac{1}{M_{\text{H}_2}} + \frac{1}{M_{\text{H}_2\text{O}}}} \frac{T^{3/2}}{p \Omega_D \zeta_{\text{H}_2, \text{H}_2\text{O}}^2} , \quad [6]$$

$$D_{\text{H}_2, \text{k}} = \frac{2}{3} \left(\frac{8RT}{\pi M_{\text{H}_2}} \right)^{1/2} r . \quad [7]$$

The mean pore radius is assumed as $r = 0.75 \mu\text{m}$ in the present study, while Ω_D is the collision integral given as:

$$\Omega_D = 1.1336 \left(\frac{Tk}{\varepsilon} \right)^{-0.1814} . \quad [8]$$

When calculating the binary diffusion coefficient, an intermolecular force constant $\zeta_{\text{H}_2, \text{H}_2\text{O}}$ is taken as an arithmetic mean of ζ_{H_2} and $\zeta_{\text{H}_2\text{O}}$. Geometric mean of ε_{H_2} and $\varepsilon_{\text{H}_2\text{O}}$ is used for ε . The gas parameters are shown in Table II.

Assuming that Ni and YSZ are perfect electronic and ionic conductors, respectively, the following equations are solved in the solid phases:

$$\nabla \left(\frac{\sigma_{e^-}}{F} \nabla \tilde{\mu}_{e^-} \right) = -i_{\text{react}} , \quad [9]$$

$$\nabla \left(\frac{\sigma_{\text{O}^{2-}}}{2F} \nabla \tilde{\mu}_{\text{O}^{2-}} \right) = i_{\text{react}} , \quad [10]$$

where $\tilde{\mu}_{e^-}$ and $\tilde{\mu}_{\text{O}^{2-}}$ are the electrochemical potentials of electron and oxide ion, respectively.

The reaction current i_{reac} , which is defined at the TPB, in the RHS of Eqs. 4, 9 and 10 is calculated as²²:

$$i_{\text{reac}} = i_0 L_{\text{TPB}} \left\{ \exp\left(\frac{2F}{RT} \eta_{\text{act}}\right) - \exp\left(-\frac{F}{RT} \eta_{\text{act}}\right) \right\}. \quad [11]$$

The lineal exchange current density i_0 is fitted from the patterned anode experiments of DeBoer²³ as follows:

$$i_0 = 31.4 \times p_{\text{H}_2}^{-0.03} p_{\text{H}_2\text{O}}^{0.4} \exp\left(-\frac{1.52 \times 10^5}{RT}\right). \quad [12]$$

The numerical conditions in this study are summarized in Table III.

Overpotential Calculation

In the LBM calculation, the electrochemical potential of electron $\tilde{\mu}_{e^-}$ in the Ni phase and that of oxide ion $\tilde{\mu}_{\text{O}^{2-}}$ in the YSZ phase are solved. The local overpotential η_{local} is defined as the voltage difference between the virtual reference electrode (RE) and the working electrode (WE) which is defined in the vicinity of TPB as shown in Fig. 7:

$$\eta_{\text{local}} = E_{\text{WE/S}} - E_{\text{RE/S}} = \frac{1}{F} \left(\tilde{\mu}_{e^-, \text{RE/S}} - \tilde{\mu}_{e^-, \text{WE/S}} \right), \quad [13]$$

where $\tilde{\mu}_{e^-, \text{RE/S}}$ and $\tilde{\mu}_{e^-, \text{WE/S}}$ are the electron electrochemical potentials at the surfaces of RE and WE, respectively. The local activation overpotential η_{act} at TPB is obtained by subtracting the ohmic losses from the local overpotential η_{local} , which is written as follows:

$$\begin{aligned} \eta_{\text{act}} &= \eta_{\text{local}} - \frac{1}{F} \left(\tilde{\mu}_{e^-, \text{RE/S}} - \tilde{\mu}_{e^-, \text{lyte/RE}} \right) \\ &\quad - \frac{1}{F} \left(\tilde{\mu}_{e^-, \text{lyte/WE}} - \tilde{\mu}_{e^-, \text{WE/S}} \right) - \frac{1}{2F} \left(\tilde{\mu}_{\text{O}^{2-}, \text{lyte/RE}} - \tilde{\mu}_{\text{O}^{2-}, \text{lyte/WE}} \right) \quad [14] \\ &= -\frac{1}{2F} \left(2\tilde{\mu}_{e^-, \text{lyte/WE}} - \tilde{\mu}_{\text{O}^{2-}, \text{lyte/WE}} + \left\{ \Delta G^\circ + RT \log\left(\frac{p_{\text{H}_2\text{O}}}{p_{\text{H}_2}}\right) \right\}_{\text{RE}} \right) \end{aligned}$$

where ohmic loss in the reference electrode is zero, $\tilde{\mu}_{e^-, \text{RE/S}} - \tilde{\mu}_{e^-, \text{lyte/RE}} = 0$. In Eq. 14, the electron in the electrolyte side at the RE/electrolyte interface is assumed to be in equilibrium with that in the electrode side $\tilde{\mu}_{e^-, \text{lyte/RE}}$, and also a local equilibrium²⁴ is assumed in the electrolyte:

$$\tilde{\mu}_{\text{O}^{2-}} = 2\tilde{\mu}_{\text{e}^-} + \mu_{\text{O}} , \quad [15]$$

In addition, the oxygen is assumed to be in equilibrium with the gaseous phase at RE:

$$\mu_{\text{O}} = \frac{1}{2} RT \ln p_{\text{O}_2} = \Delta G^\circ + RT \ln \left(\frac{p_{\text{H}_2\text{O}}}{p_{\text{H}_2}} \right) . \quad [16]$$

All the variables in the RHS of Eq. 14 are defined at the voxels adjacent to the TPB segment, which are solved in the LBM calculation.

The total overpotential of the anode η_{anode} is obtained by subtracting the ohmic losses of current collector (CC), electrolyte and RE from the potential difference between RE and CC. Assuming that the gas compositions are the same at CC and RE, we have:

$$\begin{aligned} \eta_{\text{anode}} &= \frac{1}{F} (\tilde{\mu}_{\text{e}^-, \text{RE/S}} - \tilde{\mu}_{\text{e}^-, \text{CC}}) - \frac{1}{F} (\tilde{\mu}_{\text{e}^-, \text{anode/CC}} - \tilde{\mu}_{\text{e}^-, \text{CC}}) \\ &\quad - \frac{1}{2F} (\tilde{\mu}_{\text{O}^{2-}, \text{lyte/RE}} - \tilde{\mu}_{\text{O}^{2-}, \text{anode/lyte}}) - \frac{1}{F} (\tilde{\mu}_{\text{e}^-, \text{RE/S}} - \tilde{\mu}_{\text{e}^-, \text{lyte/RE}}) \quad [17] \\ &= -\frac{1}{2F} \left(2\tilde{\mu}_{\text{e}^-, \text{anode/CC}} - \tilde{\mu}_{\text{O}^{2-}, \text{anode/lyte}} + \left\{ \Delta G^\circ + RT \log \left(\frac{p_{\text{H}_2\text{O}}}{p_{\text{H}_2}} \right) \right\}_{\text{CC}} \right) \end{aligned}$$

where ohmic loss in the reference electrode is zero, $\tilde{\mu}_{\text{e}^-, \text{RE/S}} - \tilde{\mu}_{\text{e}^-, \text{lyte/RE}} = 0$. The schematic of the total overpotential is shown in Fig. 8. Again, all the variables in the RHS of Eq. 17 are solved in the LBM calculation.

Computational Scheme

The LBM is used to solve Eqs. 4, 9 and 10 in each phase. For the 3D LBM simulation, D3Q15 ($i = 1-15$) or D3Q19 ($i = 1-19$) models are commonly used. However, it has been shown that, in the case of simple diffusion simulation, D3Q6 ($i = 1-6$) model can be efficiently used with a slight loss of accuracy.²⁵ So, the D3Q6 model is used in this study. The LB equation with the LBGK model in the collision term is written as follows:

$$f_i(\mathbf{x} + \mathbf{c}_i \Delta t, t + \Delta t) = f_i(\mathbf{x}, t) - \frac{1}{t^*} [f_i(\mathbf{x}, t) - f_i^{\text{eq}}(\mathbf{x}, t)] + w_i \Delta t . \quad [18]$$

In Eq. 18, f_i represents the density distribution function of gas, electron or ion with a velocity c_i in the i -th direction, and f_i^{eq} is the Maxwellian local equilibrium distribution,

$$f_i^{\text{eq}}(\mathbf{x}, t) = \frac{1}{6} \sum_{i=1}^6 f_i(\mathbf{x}, t). \quad [19]$$

The relaxation time t^* is a function of diffusion coefficient, voxel size Δx and time step Δt , and it is given as:

$$t^* = 0.5 + \frac{3D\Delta t}{\Delta x^2}, \quad [20]$$

where

$$D = \left(\frac{1 - \alpha y_{\text{H}_2}}{D_{\text{H}_2, \text{H}_2\text{O}}} + \frac{1}{D_{\text{H}_2, k}} \right)^{-1}. \quad [21]$$

In the present study, the time step Δt is chosen so that the relaxation time becomes $t^* = 0.99$. However, the DGM diffusion coefficient is not constant in the gaseous phase. So the relaxation time is changed according to the DGM diffusion coefficient. The last term of Eq. 18 is the production term calculated from the reaction current density (Eq. 11). A zero gradient condition is assumed at the boundaries of $x = 0, 8.43 \mu\text{m}$ and $y = 0, 6.2 \mu\text{m}$. At the current collector surface, constant gas composition (Dirichlet boundary) is applied. Constant electronic and ionic current flux conditions (Neumann boundary) are imposed on the current collector and electrolyte boundaries, respectively. A no-flux boundary condition is imposed on the solid phase boundaries in the porous media by applying the halfway bounceback scheme with a second-order accuracy.²⁶

Computational Results

In order to evaluate the grid dependence, 62 nm voxel data is coarsened to 124 and 248 voxels. Predicted overpotentials are compared with the experimental result of Matsui et al.¹⁸ in Fig. 9, where the temperature is 1000°C and the fuel compositions are 1.2% H₂O - 98.8 % H₂ and 10% H₂O - 90% H₂. Since very long computational time is required for the 62 nm grid simulation, only the 124 nm grid simulation is conducted for the case of 10% H₂O - 90% H₂. As can be seen from the figure, 62 and 124 nm results are nearly identical, while 248 nm result is much larger than the finer grid results. The connected electrochemically active TPB lengths calculated from 62, 124 and 248 nm voxel structures are 1.564, 1.449 and 0.885 $\mu\text{m}/\mu\text{m}^3$, respectively. Thus, the differences between calculated

results can be mainly attributed to the estimated TPB lengths. It is concluded that at least 124 nm resolution is required to obtain grid independent results for the present sample.

The prediction agrees well with the 1.2% H₂O - 98.8 % H₂ data, while it overpredicts the experimental data at 10% H₂O - 90% H₂ case. The anode overpotential drastically reduces with increasing $p_{\text{H}_2\text{O}}$ in the experiment. This trend is qualitatively reproduced by the simulation, but the prediction at 10% H₂O is nearly twice as large compared to the experimental data. It is considered that the dependence of exchange current i_0 on $p_{\text{H}_2\text{O}}$ should be one of the possible reasons for this discrepancy. Another possible reason is the gas phase diffusion modeling. A simple assumption of equi-molar diffusion with a constant total pressure might cause an error in predicting the local partial pressures of H₂ and H₂O near TPB, which affect the exchange current i_0 . In addition, it is reported that the domain size of the present sample is not sufficiently large for calculating the effective conductivities of Ni and YSZ phases.¹⁰ These possible reasons for the disagreement are presently under investigation and will be reported in the future.

The electrochemical potential distribution of oxide ion in the YSZ phase for the case of 1.2% H₂O - 98.8 % H₂ and $i = 0.7 \text{ A/cm}^2$ is shown in Fig. 10. Figure 10a clearly shows the potential drop from the electrolyte side to the current collector side. The potential distribution is not uniform in the x - y cross section as shown in Fig. 10b. Some grains show nearly uniform potential distribution, but others have large potential gradient inside. This is because of the scattered TPBs around the YSZ grains. Figure 11 shows the oxide ion electrochemical potential differences from the current collector $\tilde{\mu}_{\text{O}^{2-}} - \tilde{\mu}_{\text{O}^{2-}, \text{CC}}$ for $i = 0.7 \text{ A/m}^2$. The actual electrochemical potential values at 10% H₂O should be smaller than those shown in Fig. 11, since the experimental activation overpotential is much smaller than the prediction as shown in Fig. 9. The bars in the figure indicate the standard deviations at the corresponding cross sectional plane. They are around 10–30% of the mean values. The variations are larger near the electrolyte anode interface ($z < 10 \text{ }\mu\text{m}$) where electrochemical reaction at TPB is active. This large variation can be attributed to the non-uniformity of scattered TPBs, and also to the non-uniform oxide ion transport path through the YSZ phase.

Figure 12 shows local ionic and electronic current density vectors inside the solid phases at 1.2% H₂O - 98.8 % H₂ and $i = 0.7 \text{ A/cm}^2$. Note that the directions of current vectors and those of the ionic

and electronic fluxes are in the opposite directions, i.e. the current flows from the current collector to the electrolyte. The magnitudes and directions of ionic and electronic current vectors are highly distributed. The ionic and electronic currents concentrate locally at the TPB and at the neck between the solid grains. Figure 13 shows the cross sectional average values of ionic and electronic currents. The effective thickness, in which the electrochemical reaction takes place, is found to be around 10–15 μm . Humidified 10% H_2O case shows thinner effective electrode thickness than the 1.2% H_2O case, because the ionic conduction through YSZ becomes dominant compared to the electrochemical reaction at TPB. The actual effective thickness at 10% H_2O should be thinner than that found in Fig. 13, since the actual activation overpotential is much smaller than the prediction as shown in Fig. 9.

Conclusions

A three-dimensional numerical simulation of the anode overpotential is conducted in a microstructure reconstructed by FIB-SEM¹⁰. The species-transport is calculated by the LBM coupled with the electrochemical reaction at TPB. The TPB length is estimated by the centroid method, which can easily calculate the TPB length within 5% error. The predicted anode overpotential shows good agreement with the experimental data at 1.2% H_2O - 98.8 % H_2 , while the prediction overpredicts the experimental data of 10% H_2O - 90% H_2 . The dependence of exchange current density on the steam partial pressure, gas diffusion modeling as well as computational domain size remains to be studied in the future. The oxide ion electrochemical potential and current density distributions show very large non-uniformity. This fact can be attributed to the non-uniform ionic and electronic transport paths through the solid phases, and also to the scattered TPBs.

Acknowledgments

This work was supported by the New Energy and Industrial Technology Development Organization (NEDO) under the Development of System and Elemental Technology on Solid Oxide Fuel Cell (SOFC) Project. We would like to thank Drs. Koichi Eguchi and Toshiaki Matsui at Kyoto University for their experimental data and fruitful discussions.

List of Symbols

c	overlap ratio
C	molar concentration [mol / m ³]
D	diffusion coefficient [m ² / s]
f_i	velocity distribution function
f_i^{eq}	equilibrium velocity distribution function
i	current density [A / m ²]
i_0	exchange current density per TPB length [A / m ¹]
i_{reac}	reaction current density [A / m ³]
l	distance between the sphere centers [m]
L_{TPB}	TPB length per unit volume [1 / m ²]
N	molar flux [mol / (m ² s)]
p	pressure [Pa]
r	sphere radius [m]
t^*	relaxation time
T	temperature [K]
w_i	reaction production
z	distance from the electrolyte anode interface [m]

Greek Symbols

Δx	voxel size [m]
η	overpotential [V]
μ	chemical potential [J / mol]
$\tilde{\mu}$	electrochemical potential [J / mol]
σ	conductivity [S / m]

Subscripts & Superscripts

e^-	electron
O	oxygen
O^{2-}	oxide ion

H ₂	hydrogen
H ₂ O	water
lyte	electrolyte
CC	current collector
RE	reference electrode
WE	working electrode
S	surface

References

1. S. C. Singhal and K. Kendall, *High Temperature Solid Oxide Fuel Cells*, Elsevier (2002).
2. J. R. Wilson and S. Barnett, *Electrochem. Solid-State Lett.*, 11 (10), B181-B185 (2008).
3. N. Shikazono, Y. Sakamoto, Y. Yamaguchi and N. Kasagi, *J. Power Sources*, 193, 530-540 (2009).
4. J. R. Wilson, W. Kobsiriphat, R. Mendoza, H.-Y. Chen, J.M. Hiller, D. J. Miller, K. Thornton, P.W. Voorhees, S. B. Adler and S. Barnett, *Nature Materials*, 5, 541-544 (2006).
5. D. Gostovic, J. R. Smith, D. P. Kundinger, K. S. Jones and E. D. Wachsman, *Electrochem. Solid-State Lett.*, 10 (12), B214-B217 (2007).
6. J. R. Smith, A. Chen, D. Gostovic, D. Hickey, D. P. Kundinger, K. L. Duncan, R. T. DeHoff, K. S. Jones and E. D. Wachsman, *Solid State Ionics*, 180, 90-98 (2009).
7. J. R. Wilson, M. Gameiro, K. Mischaikow, W. Kalies, P. Voorhees and S. Barnett, *Microsc. Microanal.*, 15, 71-77 (2009).
8. J. R. Wilson, A. T. Duong, M. Gameiro, H.-Y. Chen, K. Thornton, W. Kalies, D. R. Mumm and S. Barnett, *Electrochemistry Communications*, 11, 1052-1056 (2009).
9. P. R. Shearing, J. Golbert, R. J. Chater and N. P. Brandon, *Chemical Eng. Sci.*, 64, 3928-3933 (2009).

10. H. Iwai, N. Shikazono, T. Matsui, H. Teshima, M. Kishimoto, R. Kishida, D. Hayashi, K. Matsuzaki, D. Kanno, M. Saito, H. Muroyama, K. Eguchi, N. Kasagi, H. Yoshida, submitted to *J. Power Sources* (2009).
11. J. R. Izzo, Jr., A. S. Joshi, K. N. Grew, W. K. S. Chiu, A. Tkachuk, S. H. Wang and W. Yun, *J. Electrochem. Soc.*, 155 (5), B504-B508 (2008).
12. J. Golbert, C. S. Adjiman and N. P. Brandon, *Ind. Eng. Chem. Res.*, 47, 7693-7699 (2008).
13. A. S. Joshi, K. N. Grew, A. A. Peracchio and W. K. S. Chiu, *J. Power Sources*, 164, 631-638 (2007).
14. P. Asinari, M. C. Quaglia, M. R. von Spakovsky and B. V. Kasula, *J. Power Sources*, 170, 359-375 (2007).
15. Y. Suzue, N. Shikazono and N. Kasagi, *J. Power Sources*, 184, 52-59 (2008).
16. C. L. Y. Yeong and S. Torquato, *Phys. Rev. E*, 58-1, 224-233 (1998).
17. W. K. S. Chiu, A. S. Joshi and K. N. Grew, *Eur. Phys. J. Special Topics*, 171, 159-165 (2009).
18. T. Matsui, R. Kishida, J.-Y. Kim, H. Muroyama and K. Eguchi, *ECS Trans.*, to appear (2009).
19. R. Krishna and J. A. Wesselingh, *Chem. Eng. Sci.*, 52, 861-911 (1997).
20. U. Anselmi-Tamburini, G. Chiodelli, M. Arimondi, F. Maglia, G. Spinolo and Z. A. Munir, *Solid State Ionics*, 110, 35-43 (1998).
21. J. R. Ferguson, J. M. Flard and R. Herbin, *J. Power Sources*, 58, 109-122 (1996).
22. T. Kawada, N. Sakai, H. Yokokawa and M. Dokiya, *J. Electrochem. Soc.*, 137, 3042-3047 (1990).
23. B. DeBoer, Ph.D. Thesis, University of Twente (1998).
24. J. Mizusaki, K. Amano, S. Yamauchi and K. Fueki, *Solid State Ionics*, 22, 313-322 (1987).
25. T. H. Zeiser, P. Lammers, E. Klemm, Y. W. Li, J. Bernsdorf and G. Brenner, *Chem. Eng. Sci.*, 56, 1697-1704 (2001).
26. M. A. Gallivan, D. R. Noble, J. G. Georgiadis and R. O. Buckius, *Int. J. Numer. Methods Fluids*, 25, 249-263 (1997).

Table I. TPB lengths calculated from FIB-SEM reconstructed structure

TPB length	$[\mu\text{m}/\mu\text{m}^3]$
Edge length	3.946
Midpoint	2.979
Centroid	2.556

Table II. Gas properties

Substance	M [g/mol]	ζ [Å]	ε/k [K]
H ₂	2.016	2.93	37
H ₂ O	18.015	2.65	356

Table III. Numerical conditions

Properties	Value
Operating temperature T [K]	1273
Total pressure p_t [Pa]	1.013×10^5
Fuel composition [mol%]	1.2 % H ₂ O – 98.8% H ₂ 10.0 % H ₂ O – 90.0% H ₂
Electronic conductivity ²⁰ σ_{e^-} [S/m]	$3.27 \times 10^6 - 1065.3T$
Ionic conductivity ²¹ $\sigma_{O^{2-}}$ [S/m]	$3.34 \times 10^4 \exp(-10300/T)$
Standard Gibbs free energy ΔG° [J/mol]	-177.99×10^3

List of figures

- Figure 1. Phase distinguished microscopy image, white: Ni, gray: YSZ, black: pore.
- Figure 2. Reconstructed Ni-YSZ anode microstructure, green: Ni, blue: YSZ.
- Figure 3. Schematic of computational domain, green: Ni, blue: YSZ.
- Figure 4. TPB length calculation methods. (a) One of the possible voxel arrangements, (b) Edge segment length, (c) Midpoint length and (d) Centroid length.
- Figure 5. TPB defined by two spheres.
- Figure 6. Comparison of TPB lengths by three methods. (a) $r/\Delta x = 5$, (b) $r/\Delta x = 15$ and (c) $r/\Delta x = 30$.
- Figure 7. Schematic of local overpotential at the vicinity of TPB.
- Figure 8. Schematic of total anode overpotential.
- Figure 9. Comparison of predicted anode overpotential with the experimental data.¹⁸
- Figure 10. Oxide ion electrochemical potential distribution in YSZ phase for 1.2% H₂O, $i = 0.7 \text{ A/cm}^2$ case. (a) Potential distribution at the YSZ surface, and (b) potential distribution at $z = 1.178 \text{ }\mu\text{m}$ cross section.
- Figure 11. Oxide ion electrochemical potential profiles $\tilde{\mu}_{\text{O}^{2-}} - \tilde{\mu}_{\text{O}^{2-}, \text{CC}}$ for $i = 0.7 \text{ A/cm}^2$.
- Figure 12. Local ionic and electronic current vectors for 1.2% H₂O, $i = 0.7 \text{ A/cm}^2$ case. (a) Ionic current vector in YSZ and (b) electronic current vector in Ni.
- Figure 13. Averaged ionic and electronic current densities along z axis for $i = 0.7 \text{ A/cm}^2$ case.

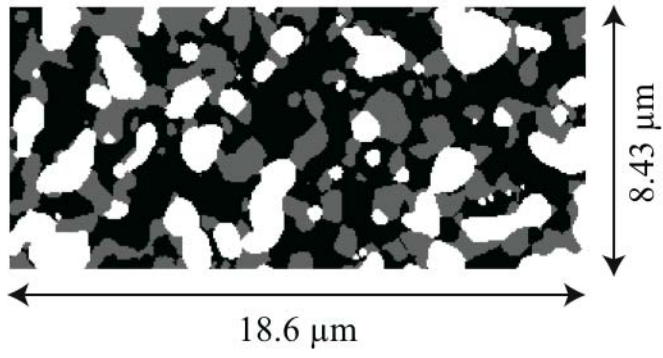


Fig. 1

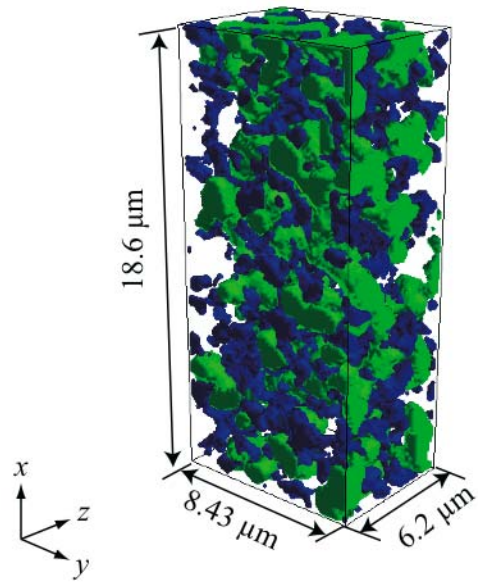


Fig. 2

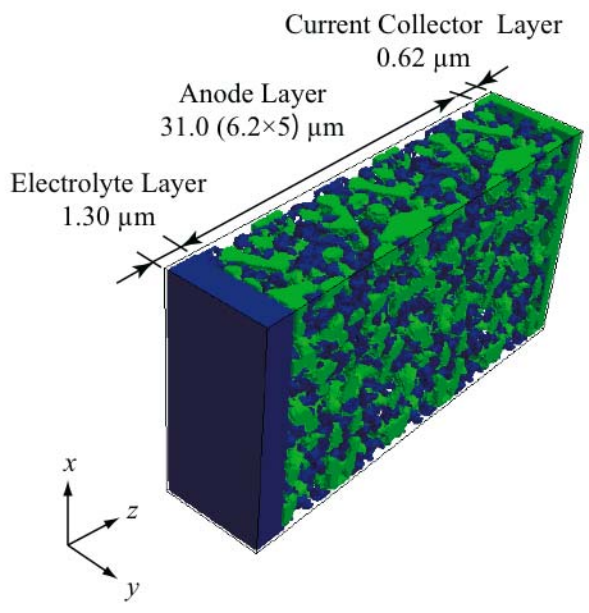
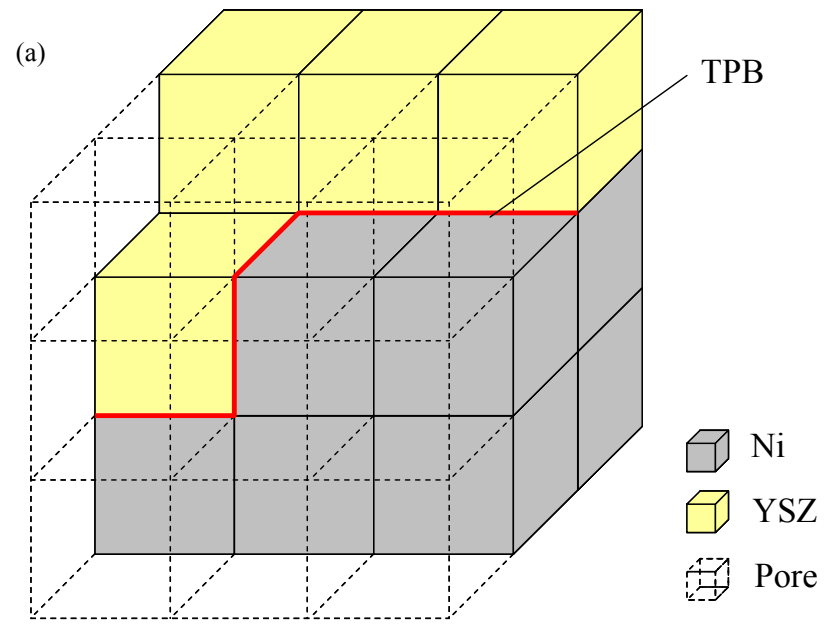


Fig. 3



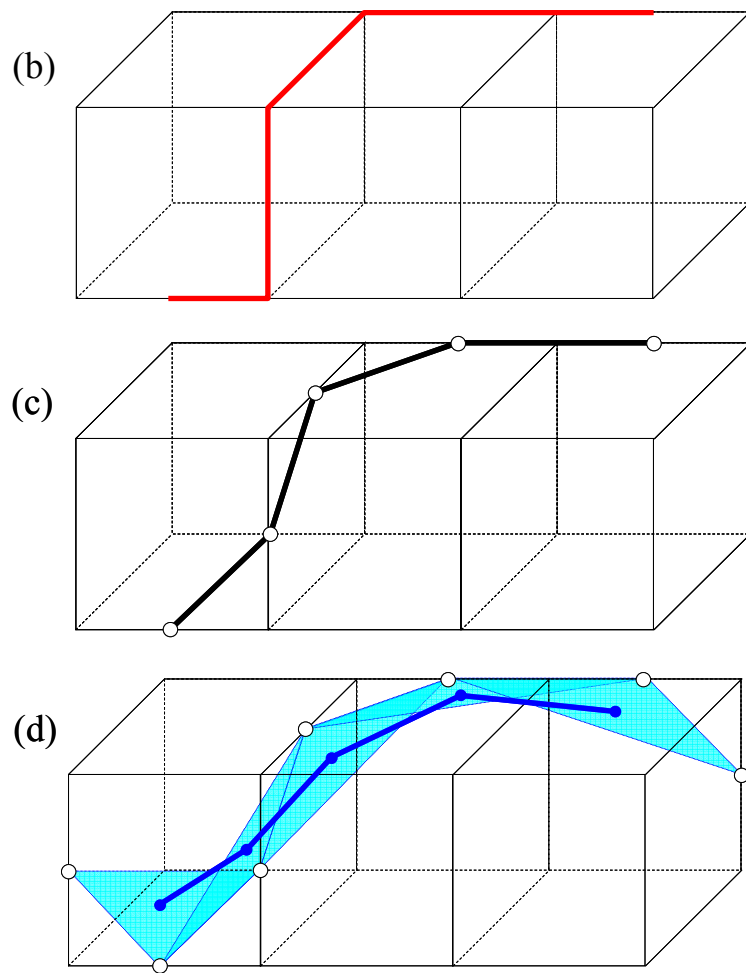


Fig. 4

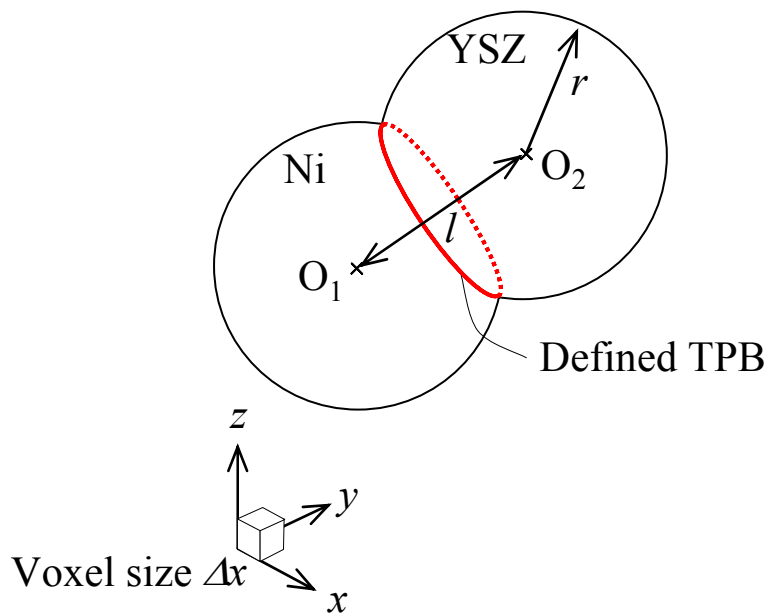
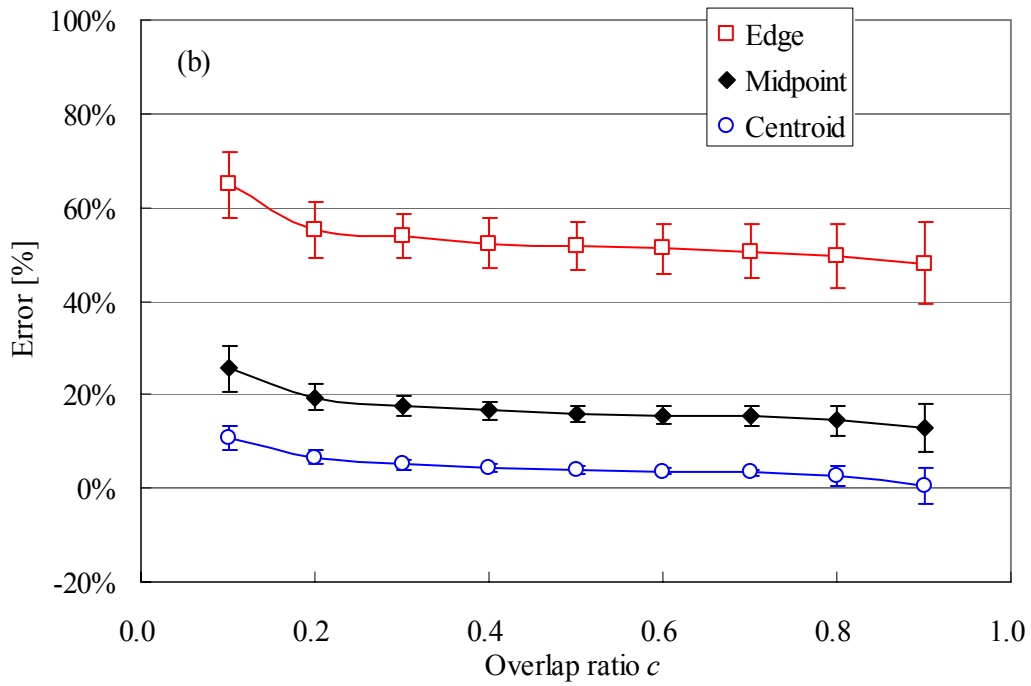
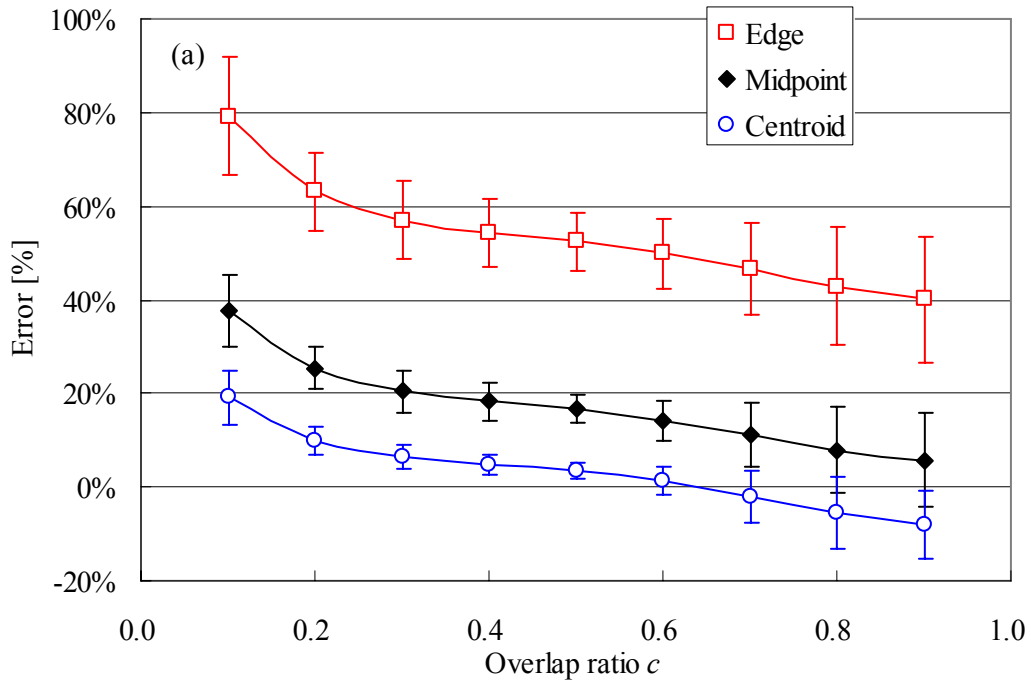


Fig. 5



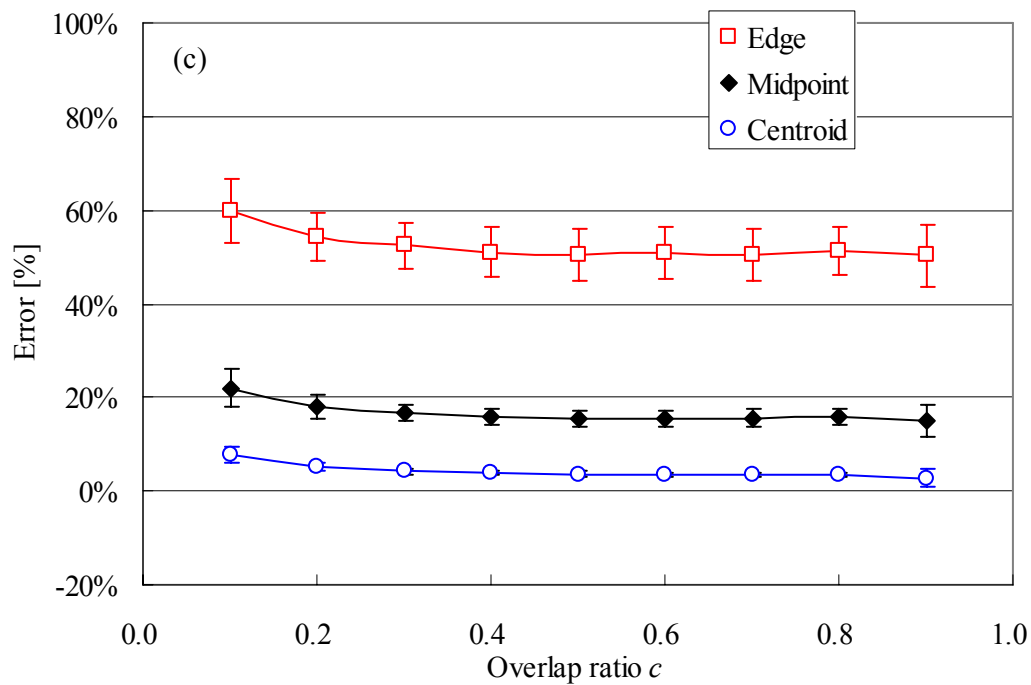


Fig. 6

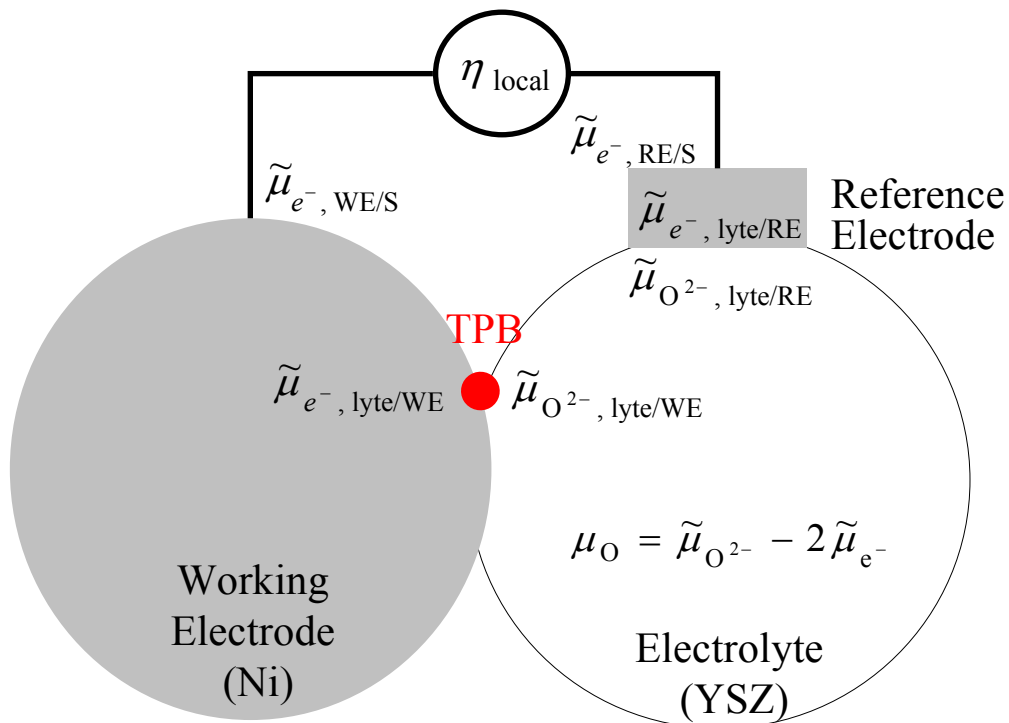


Fig. 7

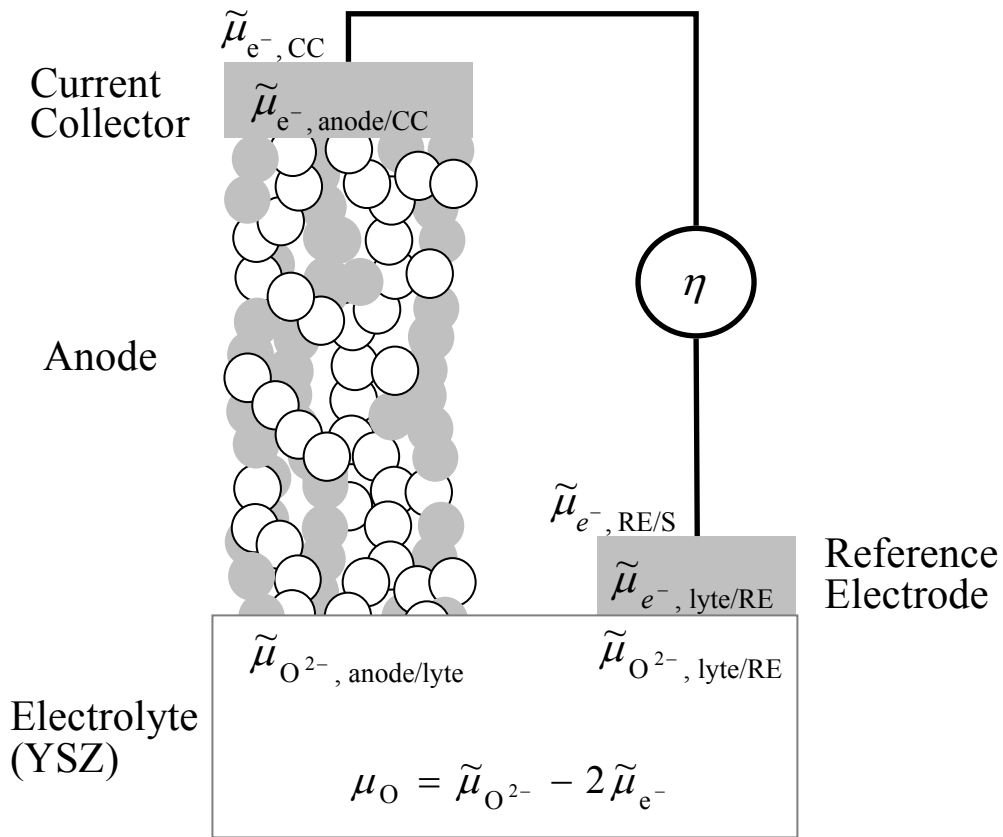


Fig. 8

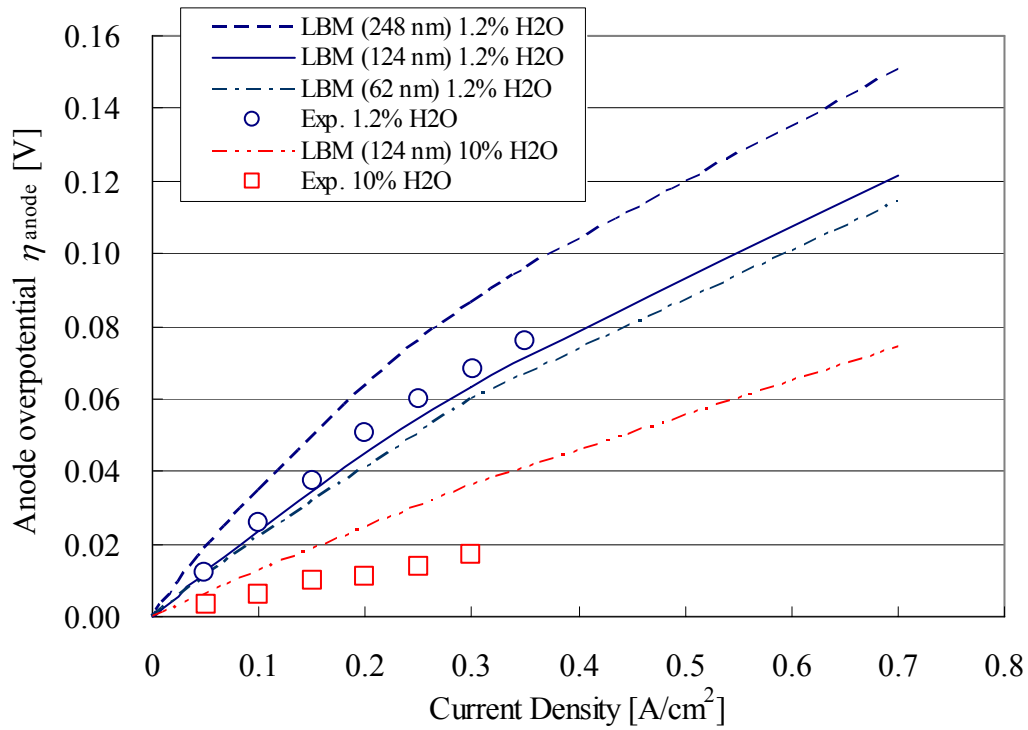
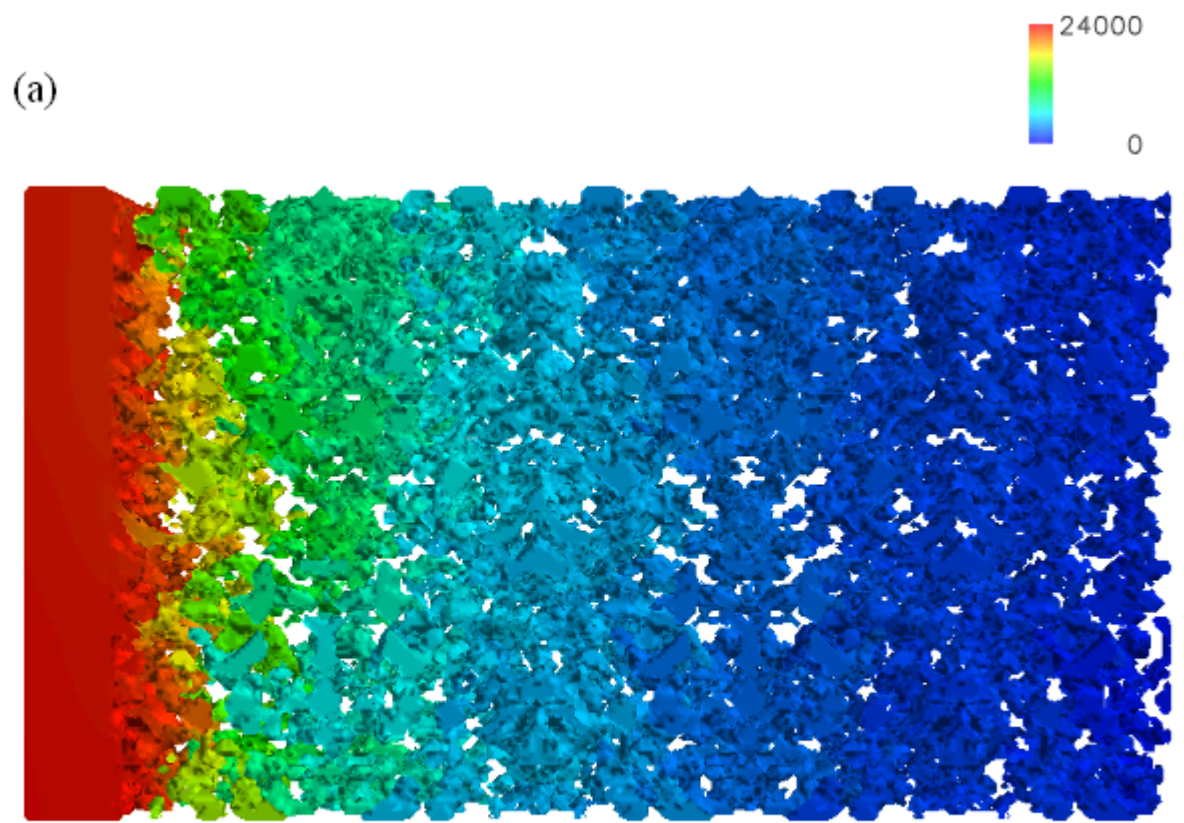


Fig. 9



(b)

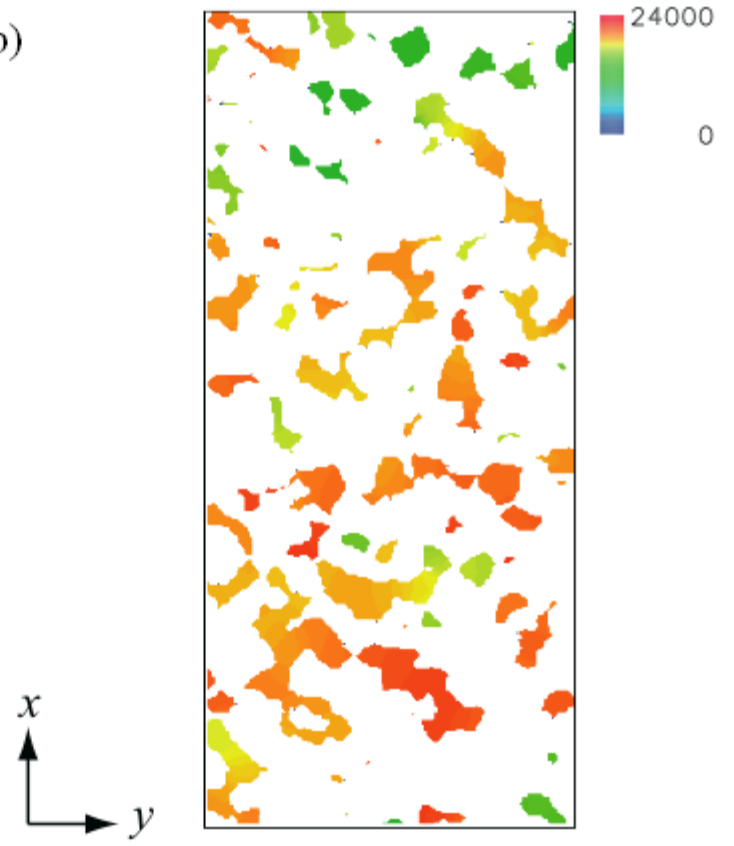


Fig. 10

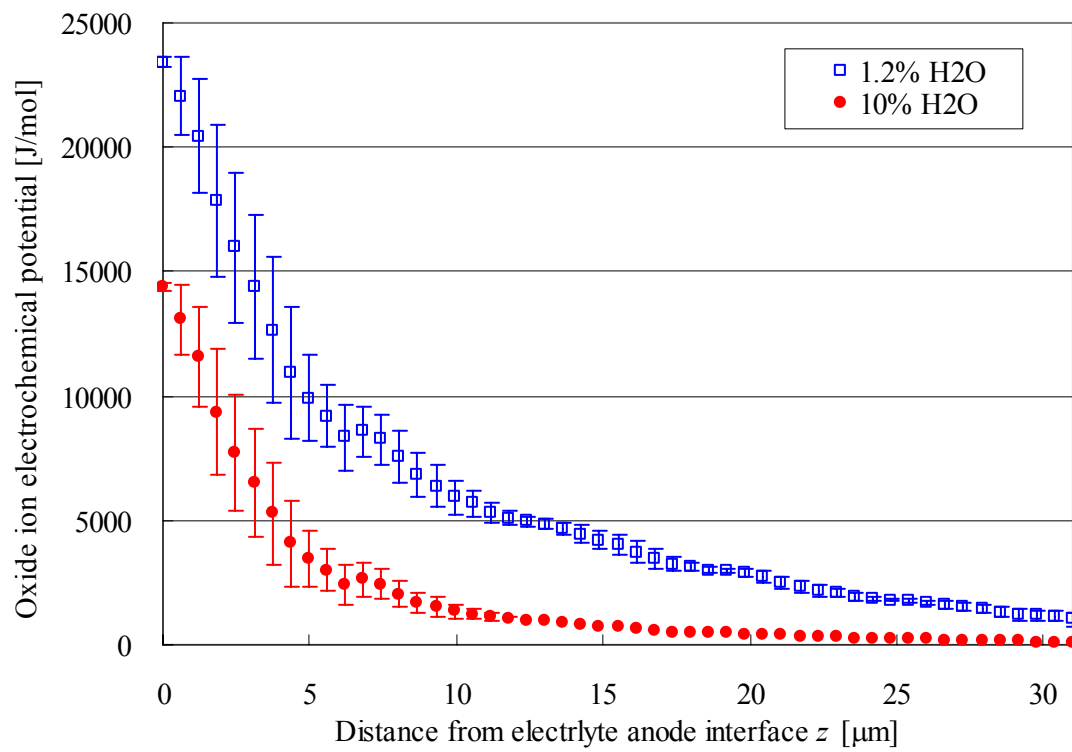
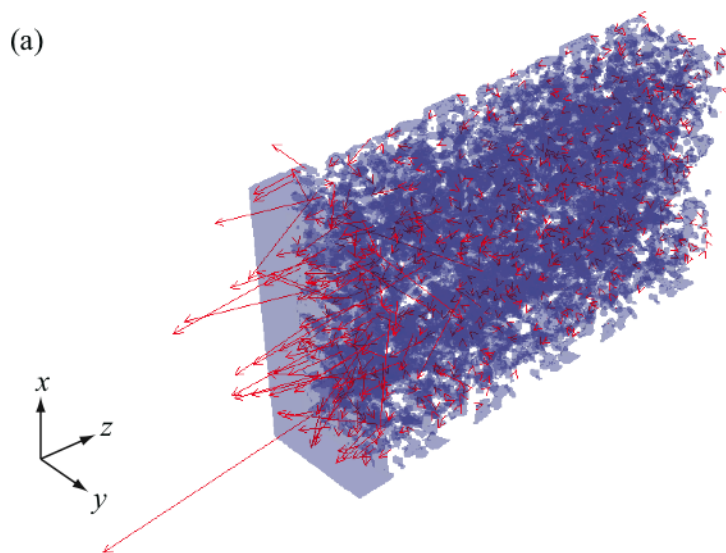


Fig. 11



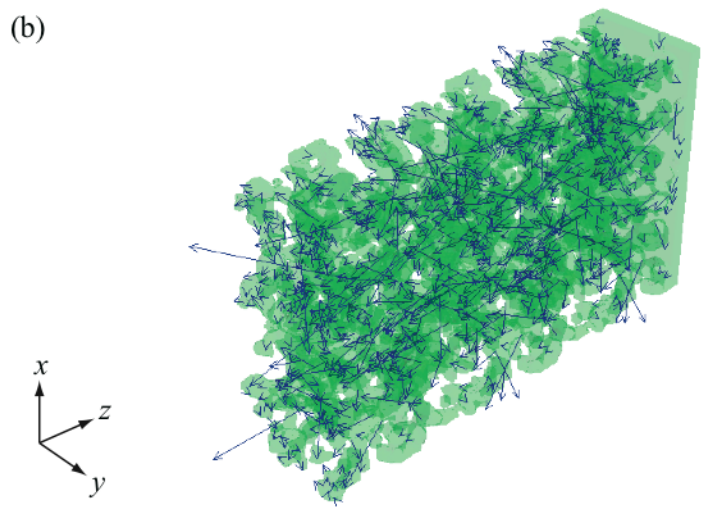


Fig. 12

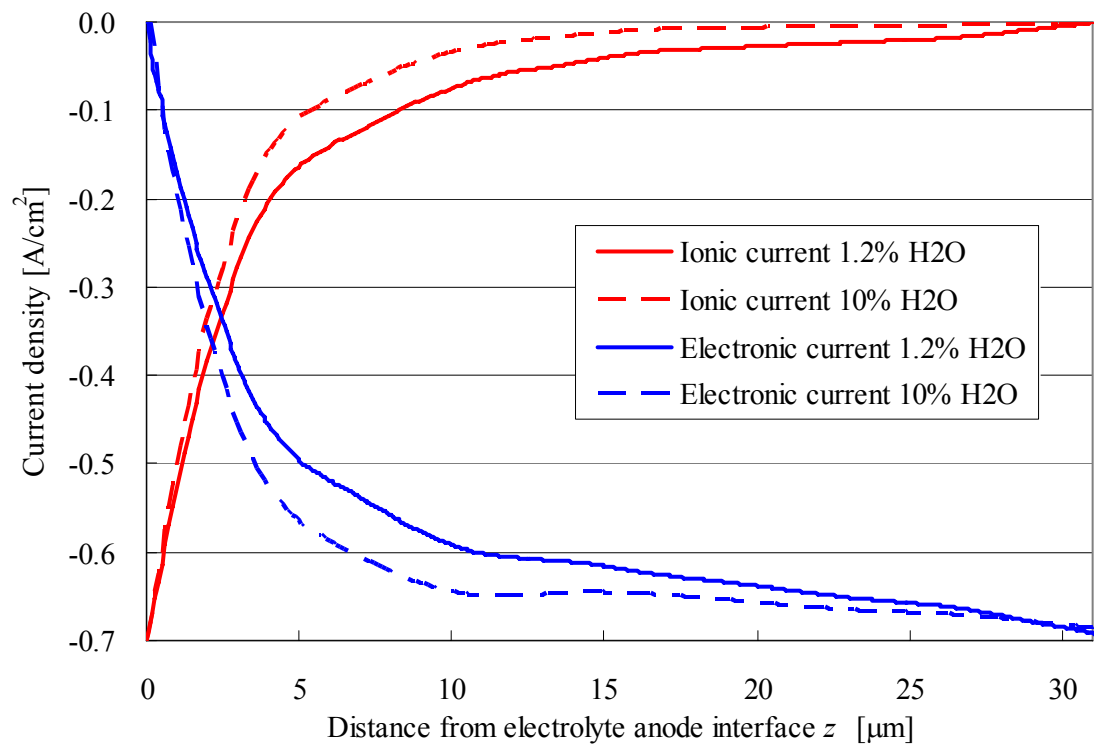


Fig. 13